Large-Area Electrodeposited WSe_2 over Graphene Electrodes for Optoelectronics

Jiapei Zhang[1], Shibin Thomas[2], Ahmad Nizamuddin Muhammad Mustafa[3,5], Victoria Greenacre[2], Nikolay Zhelev[2], Syeda Ramsha Ali[1], Yisong Han[4], Shaokai Song[1], Hongwei Zhang[1], Aiden Graham[1], Nema M. Abdelazim[1], Sami Ramadan[3], Richard Beanland[4], Gillian Reid[2], Philip N Bartlett[2], Kees de Groot[1], Yasir J Noori[1 *]

[1]School of Electronics and Computer Science, University of Southampton, Southampton SO17 1BJ, United Kingdom

[2]School of Chemistry and Chemical Engineering, University of Southampton, Southampton SO17 1BJ, United Kingdom

[3]Department of Materials, Imperial College London, London SW7 2AZ, United Kingdom

[4]Department of Physics, University of Warwick, Coventry CV4 7AL, United Kingdom

[5]FTKEK, Universiti Teknikal Malaysia Melaka, 76100 Malacca, Malaysia

[*]Authors to whom any correspondence should be addressed.

E-mail: y.j.noori@southampton.ac.uk

Keywords: electrodeposition, 2D materials, TMD, tungsten selenide, WSe_2, graphene, electrode, heterostructure

Abstract

Integrating graphene and transition metal dichalcogenides (TMDs) into layered material heterostructures brings together the exciting properties that each constituent 2D material offers. However, scaling the growth of graphene-TMD and related heterostructures remains a major challenge. In this work, we demonstrate the use of electrodeposition with a single source precursor, (SSP), $WSeCl_4$, to grow few-layer WSe_2 using graphene as an electrode. Through characterisation via photoluminescence, X-ray photoelectron and Raman spectroscopy, we show that the electrodeposited WSe_2 is stoichiometric and exhibits semiconducting and light-emitting properties. TEM imaging was also performed to show the ordering of the stacked layers of WSe_2 over graphene, demonstrating the polycrystalline structure of WSe_2. This work paves the way towards utilising electrodeposition to stack multiple TMDs, including MoS_2, WS_2 and WSe_2 over graphene for electronic and optoelectronic applications.

Introduction

Few-layer 2D transition metal dichalcogenides (TMDs) such as WSe_2 have been used to make high-performance optoelectronic devices [1-3], due to their quantum efficiency that exceeds 70% and high carrier mobility [4] [5]. Moreover, most TMDs are n-type semiconductors as deposited, while WSe_2 stands out because it is typically p-type and has been used in several demonstrations of p-n junction devices and transistors [6], making the incorporation of WSe_2 with other n-type TMDs promising for complementary metal-oxide semiconductor electronics [7].

On the other hand, graphene is a 2D material with zero band gap which offers high conductivity [8]. Therefore, graphene is widely used as an electrode material in a range of applications [9]. Specifically, in the field of flexible and transparent electronics such as field effect transistors (FETs), graphene's high conductivity, high optical transparency and stable chemical properties make it more interesting than electrode materials such as indium tin oxide (ITO) [10]. In addition to FETs, batteries [11], supercapacitors [12] and solar cells [13] have also adopted graphene as device electrodes. Given the unique individual properties of WSe_2 and graphene, integrating WSe_2 with graphene in heterostructures is very promising for various electronic and optoelectronic applications. For example, FETs that consist of WSe_2-graphene heterostructures can exhibit outstanding $I_{on/off}$ ratios [14], and photodetectors with high responsivity have been fabricated using WSe_2-graphene heterostructures [15, 16].

Exfoliation [17, 18], chemical vapor deposition (CVD) [19-21] and molecular beam epitaxy (MBE) [22-24] are common methods for depositing WSe_2 over graphene. Exfoliation can produce highly crystalline WSe_2, but it has low scalability due to depositing size-limited flakes and requiring additional transfer steps. CVD is best known for growing WSe_2 over SiO_2 and a few reports have used it to grow WSe_2 over graphene, however, the resultant films are typically discontinuous [25]. Additionally, CVD is usually not an area-selective deposition method, which would require post-deposition lithography and etching steps to pattern the grown materials, potentially creating defects and contaminating the materials [26]. In the case of MBE, the sticking coefficient of Se on the growth surface is low under ultrahigh vacuum conditions, impacting growth stoichiometry and limiting the choice of substrate [27].

An alternative method that has seldom been explored is electrodeposition. It is a room temperature technique that lends itself to depositing materials at selective areas over conductive electrodes. Electrodeposition is carried out in an electrolyte solution containing the precursor to deliver the target material. Another distinct advantage of electrodeposition lies in its ability to function as a non-line-of-sight deposition technique, enabling the conformal coating of complex three-dimensional structures, including patterned structures with high aspect ratios. Compared with the high cost and harsh deposition environment of CVD and MBE, electrodeposition is a relatively low cost technique, and it is used routinely in the semiconductor industry for the deposition of magnetic films for hard drive read/write

heads, and in the formation of Cu chip interconnects using the Damascene process [28, 29]. A few works have demonstrated the electrodeposition of tungsten diselenide (WSe_2) over conducting oxide substrate using a dual source precursor system based on H_2WO_4 and SeO_2 [30, 31]. Single source precursors (SSP) contain both the metal and the chalcogen directly bonded in a molecular species and can offer better-defined solution speciation in the electrolyte, as well as a simpler voltammetric response from the electrolyte solution. This can be beneficial for the controlled growth of mono- and few-layer TMDs, where precise control of the deposition conditions is advantageous. We have demonstrated the use of SSPs for the electrodeposition of molybdenum disulfide (MoS_2) in dichloromethane (CH_2Cl_2) using $[N^nBu_4]_2[MoS_4]$ [32, 33] and tungsten disulfide (WS_2) using $[NEt_4]_2[WS_2Cl_4]$ [34, 35].

Recently, we have also successfully electrodeposited WSe_2 2D layered thin films using $WSeCl_4$ as a SSP [36]. In this work, we exploit the same precursor to demonstrate the fabrication of a 2D heterostructure by electrodepositing WSe_2 over graphene. The presented results show, besides the novelty of graphene electrodes, an advancement in the material crystallinity and thickness control in comparison to other dual source precursor electrodeposited WSe_2 films from previous reports [30, 31]. Using a variety of characterisation techniques, we have shown that our WSe_2 exhibits semiconductor properties, demonstrating the first light emission from an electrodeposited TMD film.

2. Experimental Section

The graphene electrodes were grown by CVD on a copper foil and transferred onto a SiO_2/Si substrate using the wet transfer process [37, 38]. Thermal evaporation was used to deposit an Au film on part of the graphene film to make a solid contact pad to bias the graphene in the electrodeposition cell [32]. The precursor preparation and electrodeposition experiment were all carried out in a glove box (Belle Technology, UK) which was circulated with N_2 and maintained sub-10 ppm O_2 and H_2O levels. The detailed synthesis of the SSP, $WSeCl_4$, is given in a recent publication [39]. The solvent acetonitrile (MeCN) (Fisher, 99.9%) was dried and degassed by refluxing with CaH_2 followed by distillation. 0.1 M $[Et_4N]Cl$ (Sigma-Aldrich, ≥ 99.0%, dried *in vacuo*) was used as the supporting electrolyte. The electrodeposition was performed using a three-electrode electrochemical cell [32], where graphene was used as the working electrode, a Pt disc was used as a counter electrode, and an Ag/AgCl (in 0.1 M $[Et_4N]Cl$ in MeCN) was used as the reference electrode.

The sample thickness and roughness of WSe_2 were confirmed by tapping mode atomic force microscopy (AFM) using a Park XE7 system. The Raman spectra were obtained from a Renishaw inVia Raman spectrometer using a 532 nm wavelength laser at room temperature. Light excitation and collection were done via a 50× objective lens, which can reduce the laser spot diameter to 1 μm. The layered crystal structures of WSe_2 were measured via a JEOL ARM200f Double Aberration-Corrected transmission electron microscope (TEM) in bright and dark field mode using an acceleration voltage of

200 kV. The chemical state and stoichiometry were determined by X-ray photoelectron spectroscopy (XPS) using a Thermo Scientific Theta Probe and wavelength-dispersive X-ray spectroscopy (WDS) using an Oxford Instruments Wave Spectrometer that is coupled to a Hitachi SU70 scanning electron microscope at 10 kV. Photoluminescence Spectroscopy was measured using FLS1000 Photoluminescence Spectrometer where the material was excited via a 450 W continuous wavelength Xenon lamp.

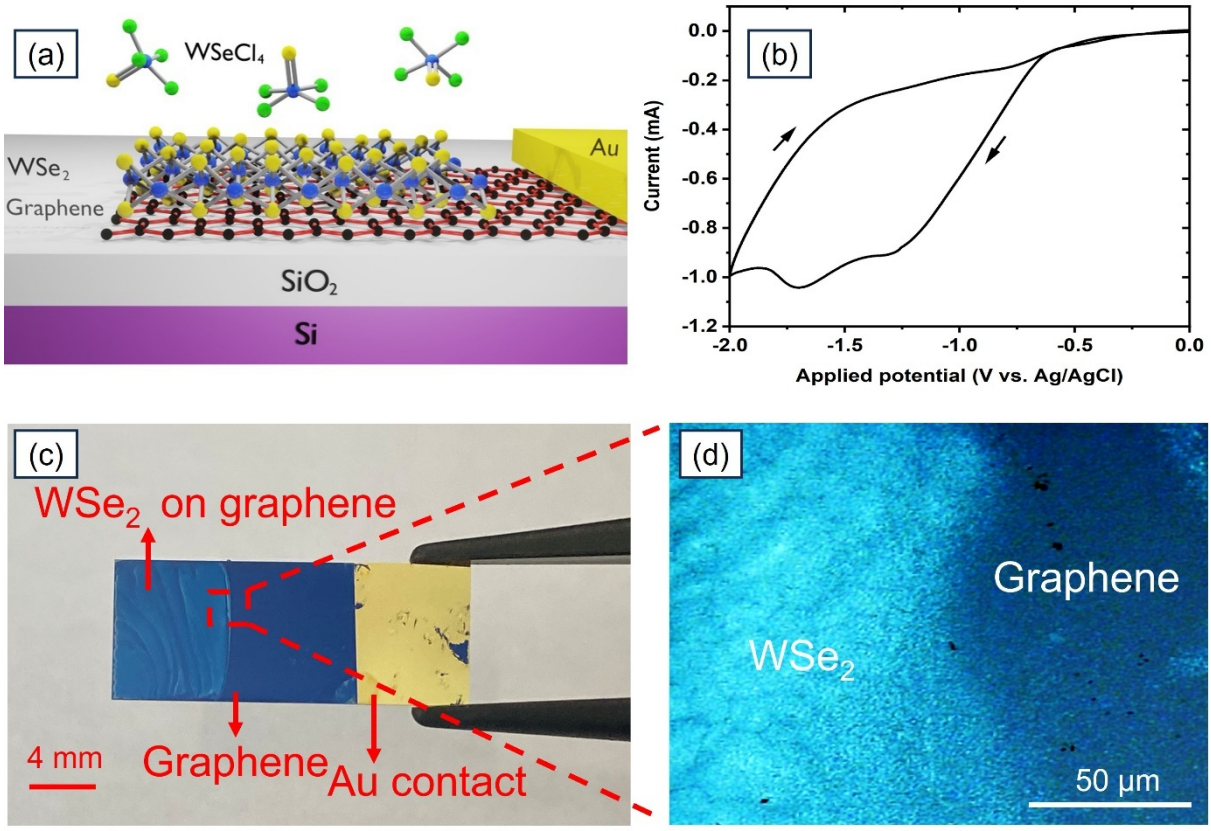

Figure 1. (a) A schematic illustration of the concept of this work showing WSe_2 electrodeposited over graphene. (b) Cyclic voltammetry scans of the 10 mM $WSeCl_4$ precursor in MeCN using a graphene electrode. Scan rate is 50 mV s^{-1} and the arrows indicate the direction of potential scanning. (c) Photograph of the graphene/SiO_2 substrate after 120 s electrodeposition, showing the area where the WSe_2 was grown over graphene and a microscope image (d) of the WSe_2 and graphene regions.

3. Results and discussion

3.1. Electrochemistry of $WSeCl_4$ on graphene

Figure 1 (a) shows a schematic image of the concept of WSe_2 electrodeposition over graphene that is presented in this paper.

The electrochemical behaviour of the [$WSeCl_4$] precursor in conjunction with the graphene working electrode was first studied by conducting cyclic voltammetry (CV) scans as shown in Figure 1 (b). The electrochemical features in the CV on graphene are comparable to the CVs recorded on TiN and Pt electrodes, which are discussed in our recent report [36]. The CV shows a clear dip in the current at around -1.4 V which correspond to the electroreduction of $WSeCl_4$ to WSe_2, and no anodic peaks are observed in the reverse scan. A plausible electrochemical reaction associated with the deposition of WSe_2 is [36]:

$$2[WSeCl_4] + 2e^- \rightarrow WSe_2 + WCl_6 + 2Cl^- \quad (\text{Eq. } 1)$$

Figure 1 (c) shows a photograph of an as-deposited large-area WSe_2 film (8 mm x 6 mm) after pulsed electrodeposition for 120 s (-1.4 V for 5 s followed by 0 V for 3 s, 24 cycles), demonstrating an obvious colour contrast to pristine graphene. Figure 1 (d) depicts a microscope image of the deposited WSe_2 film taken at the edge of the electrodeposition area, showing the uniform colour of the WSe_2 film, to give an indication of the uniformity and continuity of the deposited material. After deposition, the films are annealed at 700 °C in N_2 atmosphere in a furnace for 10 min to fully crystallise the WSe_2 film.

3.2. AFM and Raman spectroscopy

Atomic force microscope (AFM) characterisation shows that the thickness of graphene is 2-3 nm as shown by the green line in Figure 2 (a). Based on this measurement and optical microscope images from the graphene, we estimate that this represents a mono or bilayer graphene film [40]. Although the AFM measured thickness of graphene is higher than their theoretical thickness for mono and bilayers, this is typically attributed to the graphene's surface chemistry, such as the presence of solvent molecules above and below the graphene due to adsorption during the wet transfer process [41, 42]. Figure S1 shows that the 2D peak is symmetric (Figure S1 (a)), and the ratio of I_{2D}/I_G is higher than 1(Figure S1 (b)) which confirms the monolayer graphene [43]. After taking into account the 3 nm thickness (green line in Figure 2 (d)) obtained from the AFM on graphene electrodes, the 600 s deposition (-1.4 V for 5 s followed by 0 V for 3 s, 120 cycles) shows the actual as-deposited WSe_2 thickness of around 37 ± 2 nm (blue line in Figure 2 (d)), while the 120 s deposition exhibits an actual WSe_2 thickness around 4 ± 1 nm (red line in Figure 2 (d)), corresponding to around 4 to 7 layers of WSe_2 [44]. The root mean square (RMS) roughness of the 120 s deposition is 2.0 nm, which confirms much better uniformity of the electrodeposited WSe_2 films over graphene in comparison with previously reported electrodeposited WSe_2 in the literature [36]. However, further improvement to the uniformity is needed by reducing the side product formed during the electrodeposition, which has been discussed in our recent report on the electrochemistry of $WSeCl_2$ precursor and the deposition of WSe_2 on TiN [36]. Moreover, PMMA-assisted transfer process might also induce wrinkles in the graphene layer, which in turn affect uniformity of electrodeposited WSe_2 over graphene. In addition, any non-uniformity at the SiO_2 surface

can impact the adhesion and uniformity of both the transferred graphene and the subsequently electrodeposited WSe_2. Optimisation of transfer process of graphene, and improvement of electrolyte composition and electrodeposition parameters can reduce wrinkles and byproducts.

The presence of WSe_2 on the substrate, its uniformity and degree of crystallinity were investigated by measuring the Raman scattering of the film shown in Figure 3 (a). Figure 3 (b) shows the Raman spectrum of electrodeposited WSe_2, and that of a commercially grown WSe_2 bulk crystal which was used here as a reference standard is shown in Figure S2 (a). It is clear that the E^1_{2g} peak (249.5 cm^{-1}) and A_{1g} peak (257.4 cm^{-1}) are separated in the Raman spectrum of the reference sample, which is in accordance with the literature [45]. However, there is no clear separation of these peaks in the Raman spectrum of electrodeposited WSe_2, and only a major peak appears around 250 cm^{-1} which is also in accordance with reference [46]. The uniaxial strain resulting from interactions with the substrate, residual materials, and/or the electrodeposition process is responsible for the distinct separation of the Raman peaks in WSe_2. From this standpoint, monolayers are significantly influenced by strain effects, whereas thicker flakes remain largely unaffected [47]. Therefore, the reason of degeneracy of E^1_{2g} and A_{1g} peak is that the presence of uniaxial strain is weak within the multilayer electrodeposited WSe_2 which is confirmed by AFM results as shown before.

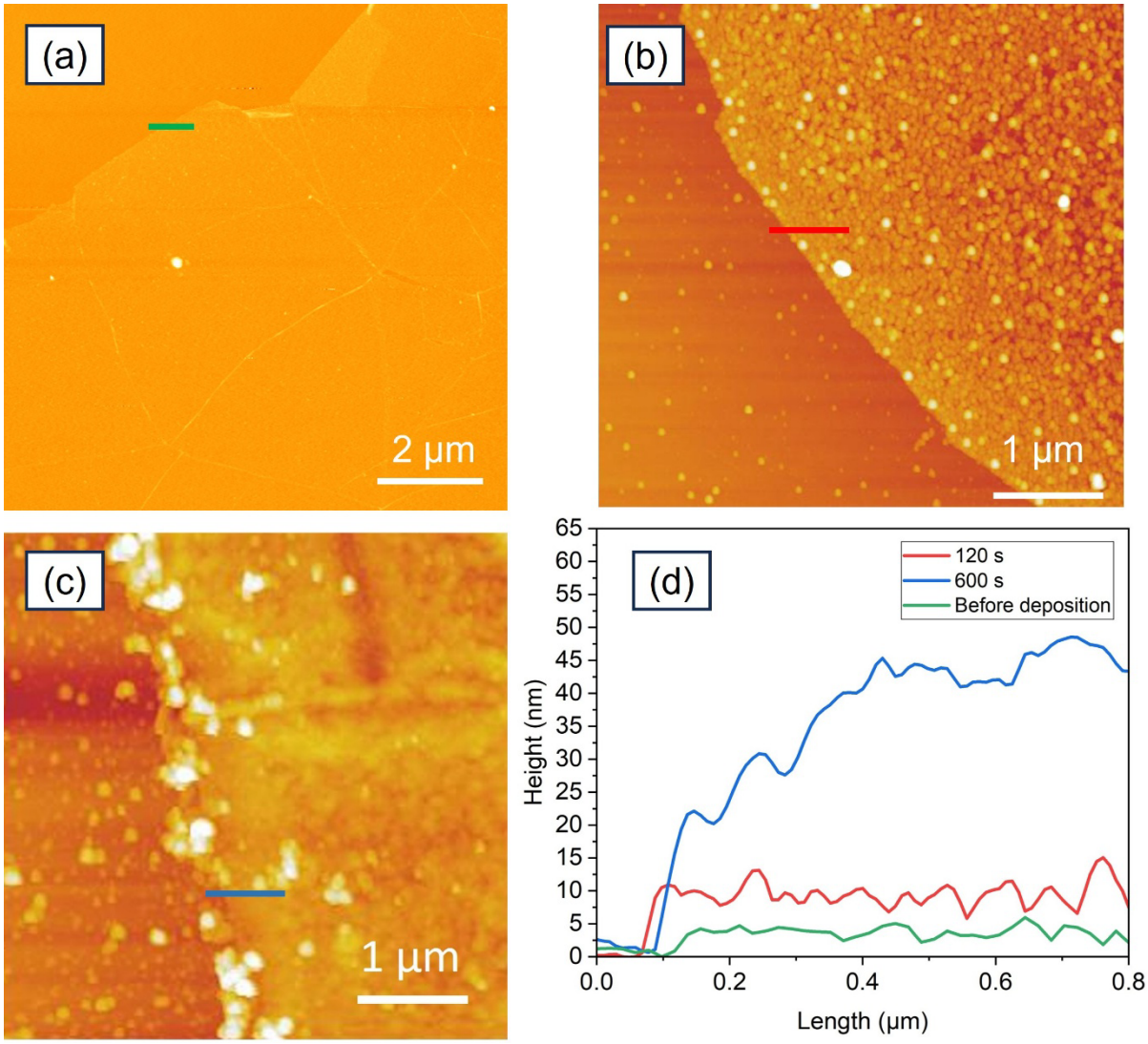

Figure 2. AFM topography images of WSe_2 deposition on graphene for (a) before deposition, (b) 120 s and (c) 600 s deposition. (d) Height profiles taken at the edges of the deposited films showing the total measured step heights.

There are three minor peaks located between 350 cm^{-1} and 400 cm^{-1} for both electrodeposited and commercial WSe_2 crystals, which are attributed to second-order Raman features that arise from exciton-phonon coupling as reported by previous experimental and theoretical calculations [48] [46]. Figure 3 (c) exhibits the WSe_2 Raman mapping image which is plotted as a function of the intensity of the Raman peak at 250 cm^{-1}. There is a significant colour contrast between the electrodeposited WSe_2 area (red) and SiO_2/Si substrate (black), and the uniform map intensity across the electrodeposition area confirms the highly uniform film. The mapping image of graphene plotted as a function of the intensity of the Raman peak at 1352 cm^{-1} (D peak of graphene) is given in Figure 3 (d). The full range Raman spectrum of both WSe_2 and graphene and Raman mapping of 2D peak are given in Figure S2 (b).

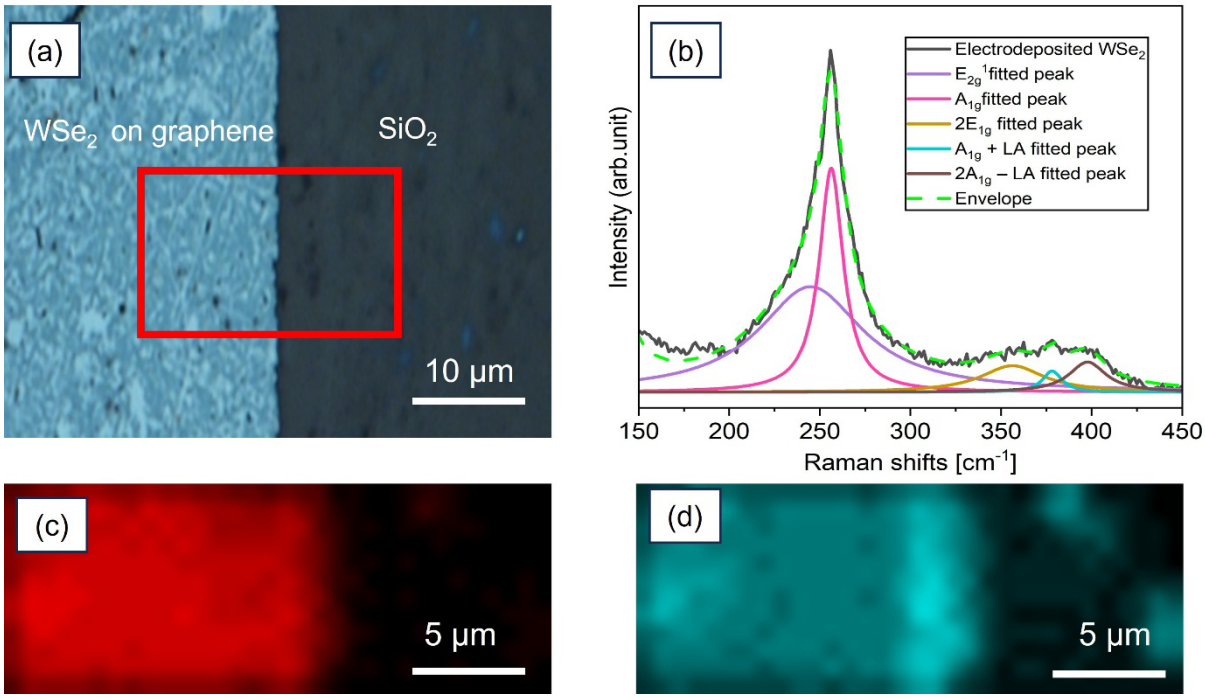

Figure 3. (a) Optical microscope image showing the contrast between the electrodeposited WSe_2 (600 s) over graphene area (left) and the underlying SiO_2/Si substrate (right). The red frame indicates the Raman mapping area for (c) and (d). (b) Raman spectra taken using a 532 nm laser of an electrodeposited WSe_2 film after annealing. Map plots for the Raman shift intensity taken at the signature peaks for (c) WSe_2 (250 cm^{-1}) and (d) graphene (1352 cm^{-1}).

3.3. TEM, XPS and WDS characterisation

TEM imaging was used to study the physical nature of the WSe_2 film, including the crystallinity, domain size and layer ordering. This is achieved by taking a lamella slice of the film using focused ion beam (FIB) milling. Pt and carbon were first deposited on the film as protection layers before the subsequent milling process. Figure 4 (a) is the TEM image under bright field (BF) mode showing the C/Pt protection layers, WSe_2, and SiO_2/Si from top to bottom. In BF mode, WSe_2 appear darker in comparison to other areas due to its constituent atoms being heavier than C, Si and O, resulting in scattering more electrons, which are blocked in BF mode. A higher magnification image of the highlighted region in (a) is presented in Figure 4 (b). We found that the film consists of ordered crystal layers that extend horizontally along the substrate and stack vertically. Figure 4 (c) shows a TEM image in dark field (DF) mode, where highly scattered electron makes the heavy WSe_2 film appear brighter. The layer-to-layer distance in the stack was measured to be 0.7 ± 0.1 nm, which matches with previously reported value [44]. TEM images of the layered WSe_2 indicate crystal domain sizes that range between 5 and 15 nm. Figure 4 (d) is the BF-TEM image of the same region shown in Figure 4 (c), with an inset showing the WSe_2 crystal under higher magnification, demonstrating its atomic structure. A guide to the eye is added showing the positions of the W (blue) and Se atoms (yellow) [49].

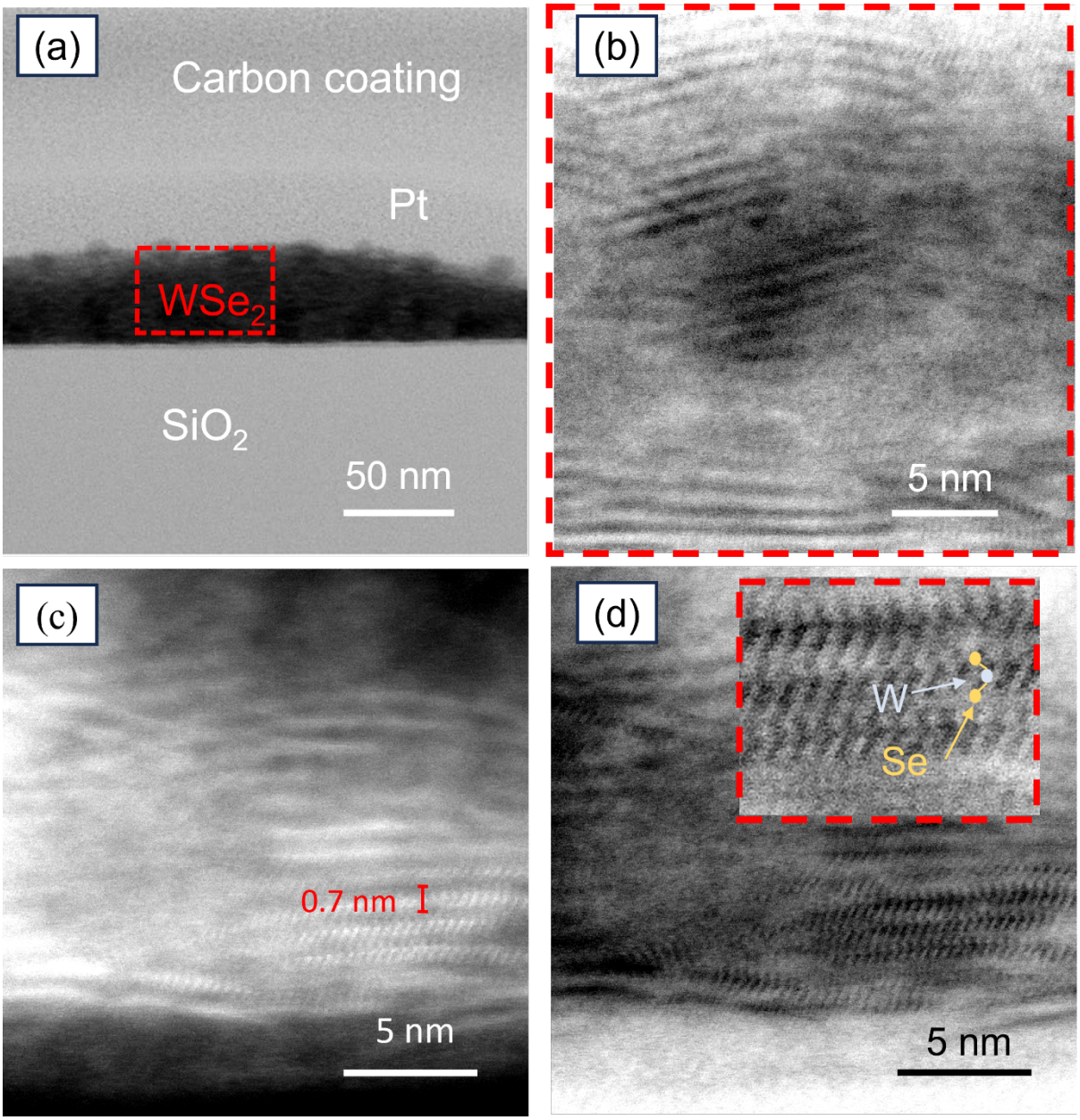

Figure 4. (a) Bright-field (BF) TEM image of electrodeposited WSe_2 films (600 s). (b) High magnification image of the highlighted region in (a) showing the layer ordering of the 2D WSe_2 growing preferentially in the horizontal direction along the surface of the substrate. (c) Dark-field (DF) TEM images of electrodeposited films (d) BF-TEM image of as same region as (c) with the inset showing the layered crystal structure of WSe_2 (blue: W atom, yellow: Se atoms).

The film composition was further investigated by XPS measurements. Figure 5 (a) shows the XPS scan of the W atoms where the two prominent peaks of $4f_{7/2}$ (32.43 eV) and $4f_{5/2}$ (34.53 eV) indicate the existence of WSe_2 [50]. The other two significant peaks of $4f_{7/2}$ (35.78 eV) and $4f_{5/2}$ (37.93 eV) belong to WO_3 [51], which can be attributed to surface oxidation from the ambient atmosphere. As shown in Figure 5 (b), the binding energies of Se^{2-} $3d_{5/2}$ and Se^{2-} $3d_{3/2}$ are 54.6 eV and 55.4 eV, respectively, which confirms the existence of WSe_2 [52][53, 54]. The W:Se composition ratio in the film is found to be

1:1.83 based on the XPS measurement. This composition agrees with our previous work on the electrodeposition of thick WSe_2 over TiN, which showed a W:Se composition ratio of 1:1.9 based on Energy Dispersive X-ray Spectroscopy (EDS) [36]. We were unable to obtain direct composition measurements from these WSe_2 over graphene samples via EDS due to the large emission spectral overlap between W (Mα = 1.774 keV) and Si (Kα = 1.739 keV). We also performed wavelength dispersive X-ray spectroscopy (WDS) as shown in Figure S3 to obtain higher resolution spectroscopy measurements, but due to the small thickness of the film, the signal-to-noise ratio was too small to obtain quantitative data.

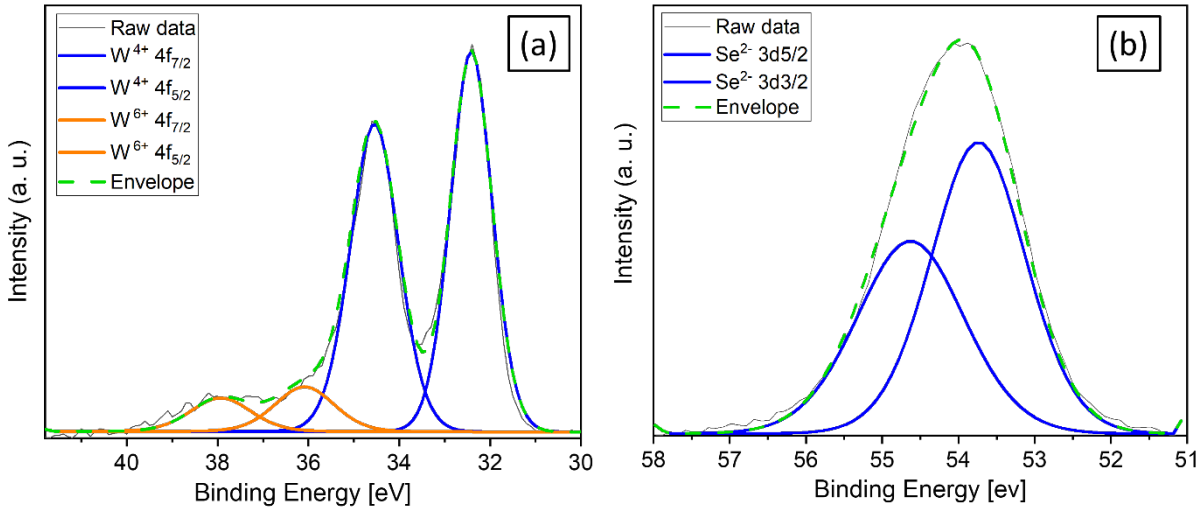

Figure 5. Large-area XPS measurements taken from the WSe_2 over graphene film (600 s) at the binding energy ranges for (a) W and (b) Se.

3.4. Photoluminescence Spectroscopy

Photoluminescence (PL) spectroscopy has been adopted to investigate the optical properties of the material and to gain insight into its quality. Figure 6 (a) displays the emission scans for graphene, electrodeposited WSe_2 over TiN and the electrodeposited WSe_2 over the graphene layer. The graphene emission scan shows almost no PL emission, as expected. The emission scan of WSe_2 on TiN and graphene display a broad PL peak centred at 710 nm with a full-width-half-maximum of 108.7 ± 4.4 nm, depicting the bandgap of the material which is one of the characteristics of WSe_2. The noticeable broad emission suggests the presence of multiple excitonic transitions that result from electronic state distribution. It should be noted that the typical PL peak of monolayer and bulk exfoliated WSe_2 is located at around 750 nm (1.65 eV) and 900 nm (1.38 eV), respectively [55-57]. It is unclear as to what causes the observed blue shift of the PL peak, but the behaviour suggests a modification of the electronic band structure. Herein, we propose that the blue shift is influenced by substrate-induced strain, dielectric screening, and charge transfer interactions. Strain effects arise from lattice mismatch and thermal

expansion differences between WSe_2 and its substrate, particularly graphene and TiN. The resulting compressive strain modifies the band structure of WSe_2, leading to an increase in its bandgap energy and a shift in PL emission toward higher energies. Previous reports have demonstrated similar bandgap modifications in strained WSe_2 films [58]. Additionally, dielectric screening plays a significant role in tuning the optical properties of WSe_2. When placed on graphene, the surrounding electronic environment changes, which can reduce exciton binding energies and modify the emission energy [59]. Another possible factor is charge transfer between WSe_2 and graphene, which can induce band structure renormalization and lead to further shifts in the optical transition energies [60].

Furthermore, Figure 6 (b) presents excitation wavelength-dependent PL measurements of the WSe_2 film over the graphene layer. The peaks of the emission and the corresponding PL intensity are extracted from Figure 6 (b) and plotted in Figure 6 (c). Both peak intensity and peak wavelength have a clear dependence on the excitation energy. The peak energy shifts from 1.82 eV to 1.72 eV with decreasing excitation energy. This is slightly higher than the typical WSe_2 monolayer/ few-layer emission at 1.65 eV. This behaviour suggests that higher excitation energy can activate additional electronic states beyond the K-point, modifying the emission characteristics [61]. The broad nature of the PL emission (>100 nm) can be attributed to defect-assisted recombination and localized excitonic states. The electrodeposition process introduces grain boundaries, vacancies, and localized trap states, all of which contribute to spectral broadening [62]. Additionally, inhomogeneous strain distribution and local potential fluctuations can result in a range of recombination energies, further widening the emission spectrum [63, 64]. The clear excitation around the bandgap energy nevertheless testifies to the semiconducting properties of the electrodeposited WSe_2, demonstrating the first reported PL emission from electrodeposited WSe_2.

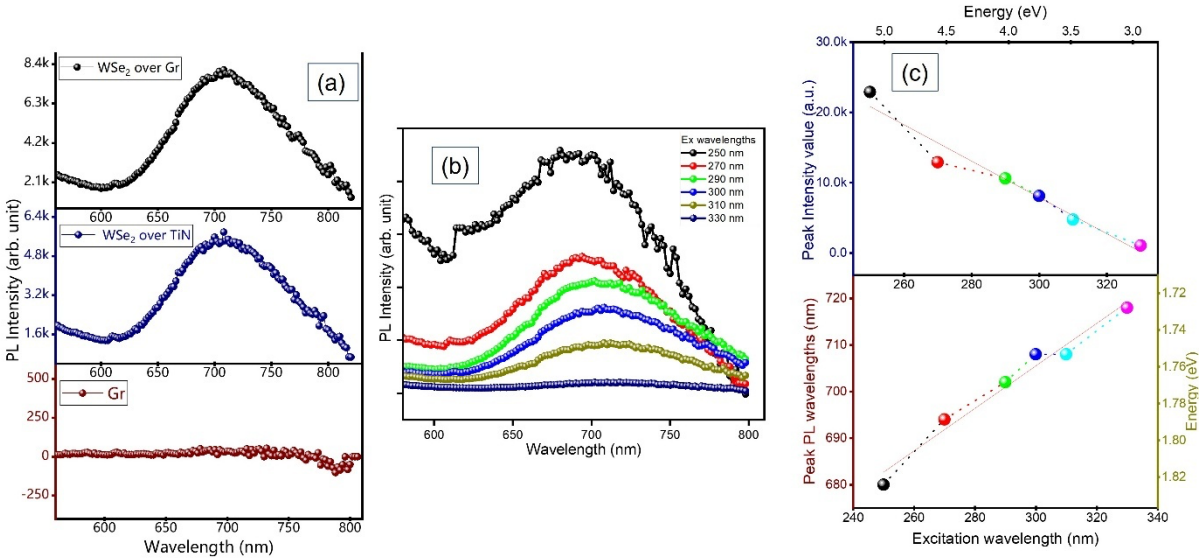

Figure 6. (a) PL scans for graphene, electrodeposited WSe_2 (600 s) on TiN and on graphene using a Xe lamp (450 W) as an excitation light source with the excitation wavelength of 300 nm. (b) Emission mapping of WSe_2 over graphene for different excitation wavelengths. (c) Plot of excitation wavelength versus peak intensity (top), and peak PL wavelength (bottom).

4. Conclusions

We report the growth of large-area WSe_2 films on graphene via electrodeposition using $WSeCl_4$ as an in-house synthesised single source precursor. The electrochemical behaviour of the precursor was investigated via cyclic voltammetry studies and a reduction potential around −1.4 V was found to be suitable for the electrodeposition of WSe_2. Raman spectroscopy was used to observe the signature of the electrodeposited film confirming the successful growth of WSe_2 and the suitability of graphene to be used as an electrode in electrodepositing this material. AFM measurements confirm that the electrodeposited WSe_2 on graphene exhibits a few-layer thickness of 4 nm with significantly higher uniformity than previously reported electrodeposited films. The W:Se composition ratio in the material is found to be 1:1.83 based on the XPS measurement and TEM imaging demonstrated the well-ordered stacks of the 2D layers and the crystal structure of WSe_2 on graphene. We then performed photoluminescence measurements to study the light emission and semiconductor properties of the electrodeposited films, which showed broad emission centred at 710 nm, demonstrating the first PL emission from an electrodeposited transition metal dichalcogenide.

Electrodeposition is a cost-effective and industry-compatible method that has the potential to scale the deposition of transition metal dichalcogenides and their heterostructures with graphene into wafer sizes. Our future work will involve adjusting the electrodeposition and annealing parameters to increase the crystal domain size to improve the PL efficiency of WSe_2 and develop p-doped electronic devices based on this material. Furthermore, this work paves the way towards utilising electrodeposition to stack multiple TMDs, including MoS_2, WS_2 and WSe_2 over graphene at wafer scales for electronic and optoelectronic applications.

Supporting information

Experiment details for graphene (Raman) and WSe_2 (Raman, AFM and WDS).

Acknowledgments

We thank the EPSRC for funding *via* the projects EP/V062689/1, EP/V062387/1, EP/V062603/1 and EP/V007629/1 and the Chemical Nanoanalysis Scanning Electron Microscopy facility at the University of Southampton.

References

[1] Zheng, Z.; Zhang, T.; Yao, J.; Zhang, Y.; Xu, J.; Yang, G. Flexible, transparent and ultra-broadband photodetector based on large-area WSe2 film for wearable devices. Nanotechnology 2016, 27, 225501. https://doi.org/10.1088/0957-4484/27/22/225501.

[2] Chen, J.; Wang, Q.; Sheng, Y.; Cao, G.; Yang, P.; Shan, Y.; Liao, F.; Muhammad, Z.; Bao, W.; Hu, L. High-performance WSe2 photodetector based on a laser-induced p–n junction. ACS Appl. Mater. Interfaces 2019, 11, 43330-43336. https://doi.org/10.1021/acsami.9b13948.

[3] Pataniya, P.; Zankat, C K.; Tannarana, M.; Sumesh, C.; Narayan, S.; Solanki, G.; Patel, K.; Pathak, V.; Jha, P K. based flexible photodetector functionalized by WSe2 nanodots. ACS Appl. Nano Mater 2019, 2, 2758-2766. https://doi.org/10.1021/acsanm.9b00266.

[4] Nguyen, D A.; Oh, H M.; Duong, N T.; Bang, S.; Yoon, S J.; Jeong, M S. Highly enhanced photoresponsivity of a monolayer WSe2 photodetector with nitrogen-doped graphene quantum dots. ACS Appl. Mater. Interfaces 2018, 10, 10322-10329. https://doi.org/10.1021/acsami.7b18419.

[5] Zou, Y.; Zhang, Z.; Yan, J.; Lin, L.; Huang, G.; Tan, Y.; You, Z.; Li, P. High-temperature flexible WSe2 photodetectors with ultrahigh photoresponsivity. Nat. Commun. 2022, 13, 4372. https://doi.org/10.1038/s41467-022-32062-0.

[6] Zhou, H.; Wang, C.; Shaw, J C.; Cheng, R.; Chen, Y.; Huang, X.; Liu, Y.; Weiss, N O.; Lin, Z.; Huang, Y. Large area growth and electrical properties of p-type WSe2 atomic layers. Nano letters 2015, 15, 709-713.

[7] Tang, H-L.; Chiu, M-H.; Tseng, C-C.; Yang, S-H.; Hou, K-J.; Wei, S-Y.; Huang, J-K.; Lin, Y-F.; Lien, C-H.; Li, L-J. Multilayer graphene–WSe2 heterostructures for WSe2 transistors. ACS Nano 2017, 11, 12817-12823. https://doi.org/10.1021/acsnano.7b07755.

[8] Schmidt, J.; Kesselman, E.; Cohen, Y.; Talmon, Y.; Tour, J M.; Pasquali, M. Spontaneous high-concentration dispersions and liquid crystals of graphene. Nature Nanotech. 2010, 5, 406-411. https://doi.org/10.1038/Nnano.2010.86.

[9] Yoon, J.; Park, W.; Bae, G Y.; Kim, Y.; Jang, H S.; Hyun, Y.; Lim, S K.; Kahng, Y H.; Hong, W K.; Lee, B H. Highly flexible and transparent multilayer MoS2 transistors with graphene electrodes. Small 2013, 9, 3295-3300. https://doi.org/10.1002/smll.201300134.

[10] Lee, W H.; Park, J.; Sim, S H.; Jo, S B.; Kim, K S.; Hong, B H.; Cho, K. Transparent flexible organic transistors based on monolayer graphene electrodes on plastic. Adv. Mater. 2011, 23, 1752. https://doi.org/10.1002/adma.201004099.

[11] Cai, X.; Lai, L.; Shen, Z.; Lin, J. Graphene and graphene-based composites as Li-ion battery electrode materials and their application in full cells. J. Mater. Chem. A 2017, 5, 15423-15446. https://doi.org/10.1039/C7TA04354F.

[12] Zhang, J.; Jiang, J.; Li, H.; Zhao, X. A high-performance asymmetric supercapacitor fabricated with graphene-based electrodes. Energy Environ. Sci. 2011, 4, 4009-4015. https://doi.org/10.1039/C1EE01354H.

[13] You, P.; Liu, Z.; Tai, Q.; Liu, S.; Yan, F. Efficient semitransparent perovskite solar cells with graphene electrodes. Adv. Mater. 2015, 27, 3632-3638. https://doi.org/10.1002/adma.201501145.

[14] Lien, C.; Tang, H-L.; Chiu, M-H.; Hou, K-J.; Yang, S-H.; Su, J-F.; Lin, Y-F.; Li, L-J. High Performance WSe2 Transistors with Multilayer Graphene Source/Drain. 2018 14th IEEE ICSICT 2018, 1-3. https://doi.org/10.1109/ICSICT.2018.8565030.

[15] Chen, T.; Sheng, Y.; Zhou, Y.; Chang, R-j.; Wang, X.; Huang, H.; Zhang, Q.; Hou, L.; Warner, J H. High photoresponsivity in ultrathin 2D lateral graphene: WS2: graphene photodetectors using direct CVD growth. ACS Appl. Mater. Interfaces 2019, 11, 6421-6430. https://doi.org/10.1021/acsami.8b20321.

[16] Tong, L.; Su, C.; Li, H.; Wang, X.; Fan, W.; Wang, Q.; Kunsági-Máté, S.; Yan, H.; Yin, S. Self-driven Gr/WSe2/Gr photodetector with high performance based on asymmetric Schottky van der Waals contacts. ACS Appl. Mater. Interfaces 2023, 15, 57868-57878. https://doi.org/10.1021/acsami.3c14331.

[17] Kim, K.; Larentis, S.; Fallahazad, B.; Lee, K.; Xue, J.; Dillen, D C.; Corbet, C M.; Tutuc, E. Band alignment in WSe2–graphene heterostructures. ACS Nano 2015, 9, 4527-4532. https://doi.org/10.1021/acsnano.5b01114.

[18] Sun, Y.; Lin, Y.; Zubair, A.; Xie, D.; Palacios, T. WSe2/graphene heterojunction synaptic phototransistor with both electrically and optically tunable plasticity. 2D Mater. 2021, 8, 035034. https://doi.org/10.1088/2053-1583/abfa6a.

[19] Huet, B.; Bachu, S.; Alem, N.; Snyder, D W.; Redwing, J M. MOCVD of WSe2 crystals on highly crystalline single-and multi-layer CVD graphene. Carbon 2023, 202, 150-160. https://doi.org/10.1016/j.carbon.2022.10.037.

[20] Azizi, A.; Eichfeld, S.; Geschwind, G.; Zhang, K.; Jiang, B.; Mukherjee, D.; Hossain, L.; Piasecki, A F.; Kabius, B.; Robinson, J A. Freestanding van der Waals heterostructures of graphene and transition metal dichalcogenides. ACS Nano 2015, 9, 4882-4890. https://doi.org/10.1021/acsnano.5b01677.

[21] Lin, Y-C.; Li, J.; de La Barrera, S C.; Eichfeld, S M.; Nie, Y.; Addou, R.; Mende, P C.; Wallace, R M.; Cho, K.; Feenstra, R M. Tuning electronic transport in epitaxial graphene-based van der Waals heterostructures. Nanoscale 2016, 8, 8947-8954. https://doi.org/10.1039/c6nr01902a.

[22] Park, J H.; Vishwanath, S.; Liu, X.; Zhou, H.; Eichfeld, S M.; Fullerton-Shirey, S K.; Robinson, J A.; Feenstra, R M.; Furdyna, J.; Jena, D. Scanning tunneling microscopy and spectroscopy of air exposure effects on molecular beam epitaxy grown WSe2 monolayers and bilayers. ACS Nano 2016, 10, 4258-4267. https://doi.org/10.1021/acsnano.5b07698.

[23] Lu, H.; Liu, W.; Wang, H.; Liu, X.; Zhang, Y.; Yang, D.; Pi, X. Molecular beam epitaxy growth and scanning tunneling microscopy study of 2D layered materials on epitaxial graphene/silicon carbide. Nanotechnology 2023, 34, 132001. https://doi.org/10.1088/1361-6528/acae28.

[24] Zhang, Y.; Xie, X.; Zong, J.; Chen, W.; Yu, F.; Tian, Q.; Meng, Q.; Wang, C.; Zhang, Y. Charge transfer between the epitaxial monolayer WSe2 films and graphene substrates. Appl. Phys. Lett. 2021, 119, 111602. https://doi.org/10.1063/5.0058538.

[25] Cheng, Q.; Pang, J.; Sun, D.; Wang, J.; Zhang, S.; Liu, F.; Chen, Y.; Yang, R.; Liang, N.; Lu, X. WSe2 2D p-type semiconductor-based electronic devices for information technology: design, preparation, and applications. InfoMat 2020, 2, 656-697. https://doi.org/10.1002/inf2.12093.

[26] Liu, F.; Shi, J.; Xu, J.; Han, N.; Cheng, Y.; Huang, W. Site-selective growth of two-dimensional materials: strategies and applications. Nanoscale 2022, 14, 9946-9962. https://doi.org/10.1039/d2nr02093a.

[27] Choudhury, T H.; Zhang, X.; Al Balushi, Z Y.; Chubarov, M.; Redwing, J M. Epitaxial growth of two-dimensional layered transition metal dichalcogenides. Annu. Rev. Mater. Res. 2020, 50, 155-177. https://doi.org/10.1146/annurev-matsci-090519-113456.

[28] Dlubak, B.; Seneor, P.; Anane, A.; Barraud, C.; Deranlot, C.; Deneuve, D.; Servet, B.; Mattana, R.; Petroff, F.; Fert, A. Are Al2O3 and MgO tunnel barriers suitable for spin injection in graphene? Appl. Phys. Lett. 2010, 97, 092502. https://doi.org/10.1063/1.3476339.

[29] Shi, J.; Liu, M.; Wen, J.; Ren, X.; Zhou, X.; Ji, Q.; Ma, D.; Zhang, Y.; Jin, C.; Chen, H. All chemical vapor deposition synthesis and intrinsic bandgap observation of MoS2/graphene heterostructures. Adv. Mater. 2015, 27, 7086-7092. https://doi.org/10.1002/adma.201503342.

[30] Delphine, S M.; Jayachandran, M.; Sanjeeviraja, C. Pulsed electrodeposition and characterisation of tungsten diselenide thin films. Mater. Chem. Phys. 2003, 81, 78-83. https://doi.org/10.1016/S0254-0584(03)00136-6.

[31] Devadasan, J J.; Sanjeeviraja, C.; Jayachandran, M. Electrosynthesis and characterisation of n-WSe2 thin films. Mater. Chem. Phys. 2003, 77, 397-401. https://doi.org/10.1016/S0254-0584(02)00095-0

[32] Noori, Y J.; Thomas, S.; Ramadan, S.; Smith, D E.; Greenacre, V K.; Abdelazim, N.; Han, Y.; Beanland, R.; Hector, A L.; Klein, N. Large-area electrodeposition of few-layer MoS2 on graphene for 2D material heterostructures. ACS Appl. Mater. Interfaces 2020, 12, 49786-49794. https://doi.org/10.1021/acsami.0c14777.

[33] Thomas, S.; Smith, D E.; Greenacre, V K.; Noori, Y J.; Hector, A L.; de Groot, C K.; Reid, G.; Bartlett, P N. Electrodeposition of MoS2 from dichloromethane. J. Electrochem. Soc. 2020, 167, 106511. https://doi.org/10.1149/1945-7111/ab9c88.

[34] Noori, Y.; Thomas, S.; Ramadan, S.; Greenacre, V.; Abdelazim, N.; Han, Y.; Zhang, J.; Beanland, R.; Hector, A L.; Klein, N. Electrodeposited WS2 monolayers on patterned graphene. 2D Mater. 2021, 9, 015025. https://doi.org/10.1088/2053-1583/ac3dd6.

[35] Thomas, S.; Greenacre, V K.; Smith, D E.; Noori, Y J.; Abdelazim, N M.; Hector, A L.; de Groot, C K.; Levason, W.; Bartlett, P N.; Reid, G. Tungsten disulfide thin films via electrodeposition from a single source precursor. Chem. Commun. 2021, 57, 10194-10197. https://doi.org/10.1039/d1cc03297f.

[36] Thomas, S.; Greenacre, V K.; Zhang, J.; Zhelev, N.; Ramadan, S.; Han, Y.; Beanland, R.; Abdelazim, N.; Noori, Y J.; de Groot, K. Electrodeposition of 2D layered tungsten diselenide thin films using a single source precursor. J. Mater. Chem. C 2024, 12, 19191-19199. https://doi.org/10.1039/d4tc02755h.

[37] Goniszewski, S.; Adabi, M.; Shaforost, O.; Hanham, S.; Hao, L.; Klein, N. Correlation of p-doping in CVD Graphene with Substrate Surface Charges. Sci. Rep. 2016, 6, 22858. https://doi.org/10.1038/srep22858.

[38] Ramadan, S.; Zhang, Y.; Tsang, D K H.; Shaforost, O.; Xu, L.; Bower, R.; Dunlop, I E.; Petrov, P K.; Klein, N. Enhancing structural properties and performance of graphene-based devices using self-assembled HMDS monolayers. ACS Omega 2021, 6, 4767-4775. https://doi.org/10.1021/acsomega.0c05631.

[39] Greenacre, V K.; Hector, A L.; Huang, R.; Levason, W.; Sethi, V.; Reid, G. Tungsten (vi) selenide tetrachloride, WSeCl 4–synthesis, properties, coordination complexes and application of [WSeCl 4 (Se n Bu 2)] for CVD growth of WSe 2 thin films. Dalton Trans. 2022, 51, 2400-2412. https://doi.org/10.1039/d1dt03980f.

[40] Li, H.; Wu, J.; Huang, X.; Lu, G.; Yang, J.; Lu, X.; Xiong, Q.; Zhang, H. Rapid and reliable thickness identification of two-dimensional nanosheets using optical microscopy. ACS Nano 2013, 7, 10344-10353. https://doi.org/10.1021/nn4047474.

[41] Ochedowski, O.; Bussmann, B K.; Schleberger, M. Graphene on mica-intercalated water trapped for life. Sci. Rep. 2014, 4, 6003. https://doi.org/10.1038/srep06003.

[42] Cao, P.; Xu, K.; Varghese, J O.; Heath, J R. Atomic force microscopy characterization of room-temperature adlayers of small organic molecules through graphene templating. J. Am. Chem. Soc. 2011, 133, 2334-2337. https://doi.org/10.1021/ja108554p.

[43] Shearer, C J.; Slattery, A D.; Stapleton, A J.; Shapter, J G.; Gibson, C T. Accurate thickness measurement of graphene. Nanotechnology 2016, 27, 125704. https://doi.org/10.1088/0957-4484/27/12/125704.

[44] Chen, J-W.; Lo, S-T.; Ho, S-C.; Wong, S-S.; Vu, T-H-Y.; Zhang, X-Q.; Liu, Y-D.; Chiou, Y-Y.; Chen, Y-X.; Yang, J-C. A gate-free monolayer WSe2 pn diode. Nat. Commun. 2018, 9, 3143. https://doi.org/10.1038/s41467-018-05326-x.

[45] Zeng, H.; Liu, G-B.; Dai, J.; Yan, Y.; Zhu, B.; He, R.; Xie, L.; Xu, S.; Chen, X.; Yao, W. Optical signature of symmetry variations and spin-valley coupling in atomically thin tungsten dichalcogenides. Sci. Rep. 2013, 3, 1608. https://doi.org/10.1038/srep01608.

[46] Del Corro, E.; Terrones, H.; Elias, A.; Fantini, C.; Feng, S.; Nguyen, M A.; Mallouk, T E.; Terrones, M.; Pimenta, M A. Excited excitonic states in 1L, 2L, 3L, and bulk WSe2 observed by resonant Raman spectroscopy. ACS Nano 2014, 8, 9629-9635. https://doi.org/10.1021/nn504088g.

[47] Sahin, H.; Tongay, S.; Horzum, S.; Fan, W.; Zhou, J.; Li, J.; Wu, J.; Peeters, F. Anomalous Raman spectra and thickness-dependent electronic properties of WSe 2. Phys. Rev. B 2013, 87, 165409. https://doi.org/10.1103/PhysRevB.87.165409.

[48] Li, H.; Lu, G.; Wang, Y.; Yin, Z.; Cong, C.; He, Q.; Wang, L.; Ding, F.; Yu, T.; Zhang, H. Mechanical exfoliation and characterization of single-and few-layer nanosheets of WSe2, TaS2, and TaSe2. Small 2013, 9, 1974-1981. https://doi.org/10.1002/smll.201202919.

[49] Jariwala, D.; Sangwan, V K.; Lauhon, L J.; Marks, T J.; Hersam, M C. Emerging device applications for semiconducting two-dimensional transition metal dichalcogenides. ACS Nano 2014, 8, 1102-1120. https://doi.org/10.1021/nn500064s.

[50] Sierra-Castillo, A.; Haye, E.; Acosta, S.; Bittencourt, C.; Colomer, J-F. Synthesis and characterization of highly crystalline vertically aligned WSe2 nanosheets. Appl. Sci. 2020, 10, 874. https://doi.org/10.3390/app10030874.

[51] Li, S.; Yao, Z.; Zhou, J.; Zhang, R.; Shen, H. Fabrication and characterization of WO3 thin films on silicon surface by thermal evaporation. Mater. Lett. 2017, 195, 213-216. https://doi.org/10.1016/j.matlet.2017.02.078.

[52] Zhang, B-Q.; Chen, J-S.; Niu, H-L.; Mao, C-J.; Song, J-M. Synthesis of ultrathin WSe 2 nanosheets and their high-performance catalysis for conversion of amines to imines. Nanoscale 2018, 10, 20266-20271. https://doi.org/10.1039/C8NR05954C.

[53] Chen, C.; Zhao, Y.; Lu, S.; Li, K.; Li, Y.; Yang, B.; Chen, W.; Wang, L.; Li, D.; Deng, H. Accelerated optimization of TiO2/Sb2Se3 thin film solar cells by high-throughput combinatorial approach. Adv. Energy Mater. 2017, 7, 1700866. https://doi.org/10.1002/aenm.201700866.

[54] Wang, J andGuan, F. Solution-synthesis of Sb 2 Se 3 nanorods using KSeCN as a molecular selenium source. CrystEngComm 2020, 22, 68-73. https://doi.org/10.1039/C9CE01399G.

[55] Yan, T.; Qiao, X.; Liu, X.; Tan, P.; Zhang, X. Photoluminescence properties and exciton dynamics in monolayer WSe2. Appl. Phys. Lett. 2014, 105, https://doi.org/10.1063/1.4895471.

[56] Bandyopadhyay, A S.; Biswas, C.; Kaul, A B. Light–matter interactions in two-dimensional layered WSe2 for gauging evolution of phonon dynamics. Beilstein J. Nanotechnol 2020, 11, 782-797. https://doi.org/10.3762/bjnano.11.63.

[57] Zhao, W.; Ghorannevis, Z.; Chu, L.; Toh, M.; Kloc, C.; Tan, P-H.; Eda, G. Evolution of electronic structure in atomically thin sheets of WS2 and WSe2. ACS Nano 2013, 7, 791-797. https://doi.org/10.1021/nn305275h.

[58] Desai, S B.; Seol, G.; Kang, J S.; Fang, H.; Battaglia, C.; Kapadia, R.; Ager, J W.; Guo, J.; Javey, A. Strain-induced indirect to direct bandgap transition in multilayer WSe2. Nano Lett. 2014, 14, 4592-4597. https://doi.org/10.1021/nl501638a.

[59] Liu, D.; Yan, X-Q.; Guo, H-W.; Liu, Z-B.; Zhou, W-Y.; Tian, J-G. Substrate effect on the photoluminescence of chemical vapor deposition transferred monolayer WSe2. J. Appl. Phys. 2020, 128, https://doi.org/10.1063/5.0008586.

[60] Jia, Z.; Shi, J.; Shang, Q.; Du, W.; Shan, X.; Ge, B.; Li, J.; Sui, X.; Zhong, Y.; Wang, Q. Charge-transfer-induced photoluminescence properties of WSe2 monolayer–bilayer homojunction. ACS Appl. Mater. Interfaces 2019, 11, 20566-20573. https://doi.org/10.1021/acsami.9b06017.

[61] Gupta, S.; Wu, W.; Huang, S.; Yakobson, B I. Single-photon emission from two-dimensional materials, to a brighter future. J. Phys. Chem. Lett. 2023, 14, 3274-3284. https://doi.org/10.1021/acs.jpclett.2c03674.

[62] Zalogina, A.; Li, C.; Zhigulin, I.; Coste, N.; Alijani, H.; Schaeper, O C.; Charlton, H.; Ward, J.; Ren, H.; Aharonovich, I. An Inverse Design Wavelength Demultiplexer for On-Chip Photoluminescence Sorting in TMDC Heterostructures. arXiv preprint arXiv:2501.14261 2025, https://doi.org/10.48550/arXiv.2501.14261.

[63] Sajid, M.; Qamar, M A.; Farhan, A.; Qayyum, W.; Khalid, A.; Nawaz, A.; Lee, S-l.; Nawaz, H. Emerging Paradigms in Two-Dimensional Materials: Classification, Synthesis, and the Role of Defects in Electrocatalysis for Water Splitting and Oxygen Reduction Reaction. J. Environ. Chem. Eng. 2024, 12, 113784. https://doi.org/10.1016/j.jece.2024.113784.

[64] Yue, R.; Nie, Y.; Walsh, L A.; Addou, R.; Liang, C.; Lu, N.; Barton, A T.; Zhu, H.; Che, Z.; Barrera, D. Nucleation and growth of WSe2: enabling large grain transition metal dichalcogenides. 2D Mater. 2017, 4, 045019. https://doi.org/10.1088/2053-1583/aa8ab5.